Non-contact Manipulation for Automated Protein Crystal Harvesting using a Rolling Microrobot

Roel S. Pieters [*] **Hsi-Wen Tung** [*] **David F. Sargent** [*,**]
Bradley J. Nelson [*]

[*] *Institute of Robotics and Intelligent Systems, ETH Zurich,*
Tannenstrasse 3, Zurich, 8092, Switzerland.
[**] *Institute of Molecular Biology and Biophysics, ETH Zurich,*
Schafmattstrasse 20, Zurich, 8093, Switzerland.
(rpieters@ethz.ch, bnelson@ethz.ch)

Abstract: In this work, a visual control system for magnetically-driven, automated protein crystal harvesting is proposed. The system consists of a rod-shaped microrobot, a magnetic actuation system and a visual control system. The rolling motion of the microrobot on a surface is induced by a rotating magnetic field. As the robot is submerged in a low Reynolds number liquid this motion creates a vortex above the robot which enables the non-contact transportation of protein crystals towards an extraction point. We present the micro-agent, the actuation system and the visual control system to achieve this automated procedure.

Keywords: Microsystems, robotics, magnetic fields, robot vision, automatic control

1. INTRODUCTION

X-ray crystallography is the predominant method used to determine the spatial structure of macromolecules at atomic resolution. The harvesting of these protein crystals is usually done manually, due to the small scale (the size ranges from microns to one millimeter) and delicate nature of the crystals. This causes the harvesting to be the major bottleneck of high-throughput crystallography (Tung et al., 2014a). In this work we present an approach to automate the process of protein crystal harvesting.

Technologies that have been developed to solve such micromanipulation tasks are e.g. optical or magnetic tweezers, microgrippers or wireless mobile micro-devices (for an overview, see e.g. (Banerjee and Gupta, 2013)). When considering micromanipulation via magnetic micro-devices, tasks can be executed in two ways: by direct contact or in a noncontact manner. Direct contact indicates a physical contact between the manipulation tool and the micro-object. Noncontact methods transmit force to the manipulated objects through the medium in which the micro-devices and the objects are immersed. For example, using fluid flow induced by the agent allows delicate objects to be manipulated very gently. This has been demonstrated successfully for the micromanipulation of microspheres, single cells and micro-organisms in several studies. For example, Zhang et al. (2012) trapped and transported objects by the vortices generated by tumbling nanowires, while Jiang et al. (2010) used a spinning sphere to generate a rotating flow and trap objects. A similar study on fluid-based manipulation of micro-scale objects using rotating magnetic microrobots can be found in (Diller et al., 2011),

where mobile rotating magnetic microrobots are used to manipulate micro-objects via induced fluid flow.

The visual control system presented in this work is based on classical non-holonomic techniques used for wheeled mobile robots (Laumond, 1998). This is also similar to recently reported control strategies for remote surgical tissue cutting (Staub et al., 2012). Past methods to automate the crystal harvesting process include the use of optical tweezers (Wagner et al., 2013) and robotic arms (Viola et al., 2007; Yaser et al., 2013), a recent overview of approaches can be found in (Deller and Rupp, 2014).

The method proposed in the present work uses a (rotating) magnetic field for the actuation of a microrobot. The motion of the robot generates a rising flow in front of it and a vortex above it (Tung et al., 2013). Protein crystals can then be lifted off the substrate by the flow, trapped in the vortex and transported to and deposited onto an extraction-loop (see Fig. 1). This contact-less manipulation method is extremely useful for delicate objects such as protein crystals and novel in the crystallographic community.
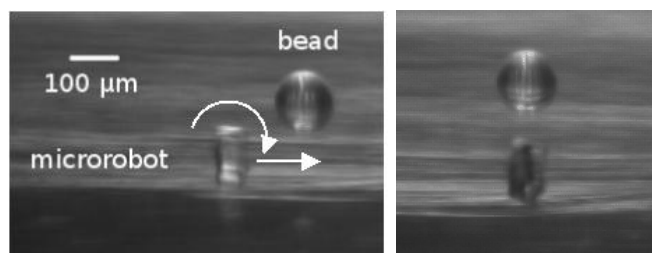

Fig. 1. Sideview of the rolling microrobot lifting up (left) and trapping (right) a polystyrene bead in the vortex.

To allow the full potential of fast and precise protein crystal harvesting, a visual and robot-assisted system has been developed to help crystallographers extract crystals automatically. This includes a magnetic manipulation system to generate forces and actuate a microrobot, and a visual control system to detect and track the robot and provide feedback for motion control. The control approach - trajectory tracking - incorporates the kinematic and non-holonomic constraints of the robot and enables a straight-forward design of motion. The input to the control system is the forward velocity of the robot and the yaw angle of the robot.

We demonstrate the effectiveness of actuating the micro-robot as well as the ability to trap micro-objects in a vortex (e.g., protein crystals). Moreover, we show the automated transportation of these to a desired location via visual feedback control.

1.1 Protein Crystal Harvesting

The harvesting of protein crystals can be a complicated task. Crystals can range in size from a few microns to several hundreds of microns, are non-uniform in size and color, and are semi-transparent. Moreover, the crystals tend to be extremely fragile and can disintegrate when removed from their growth solution. As a consequence, manual crystal harvesting is a difficult task often pushing the limits of the capabilities of the human sensory and motor system. The automation of crystal harvesting is, therefore, a logical next step towards fully automated X-ray crystallography.

The steps involved in the automation of protein crystal harvesting are as follows. To begin harvesting, a well containing the crystals is placed under a microscope, usually in a drop of mother liquor (from $< 1 \mu L$ to greater than $10 \mu L$). A small harvesting device (e.g., a MiTeGen MicroGripper^{TM} ($50 - 400 \mu m$) is then introduced into the droplet to receive the crystal for extraction (see Fig. 2). Once the crystal is retrieved, it is flash-cooled to stabilize it and prevent it from degenerating. The crystal is then analysed in an X-ray beam.
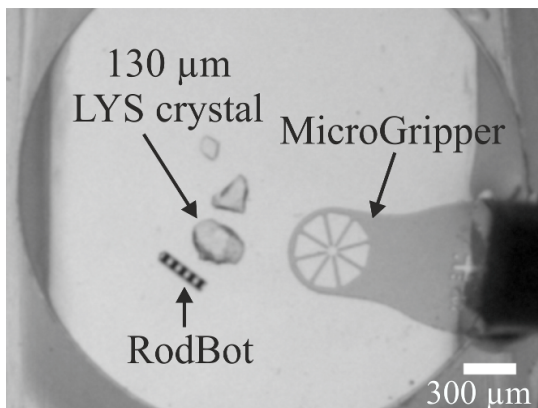

Fig. 2. Microscopic view of the proposed harvesting process. A magnetic field actuates the microrobot (Rod-Bot), which transports Lysozyme (LYS) crystals towards an extraction-tool (MicroGripper^{TM}).

Automated techniques that could improve a manual procedure are the image analysis system, the real-time guidance of the transportation of the crystal, and the automatic extraction of the crystal. The proposed visual control system automates the transportation of the crystal by controlling a microrobot with visual feedback.

This paper proceeds as follows. In Section 2 the magnetic manipulation system and the microrobot are introduced. Section 3 presents the visual control approach. An experimental evaluation of all techniques is discussed in Section 4, and Section 5 presents the conclusions.

2. MAGNETIC MOTION SYSTEM

The microrobot is exposed to an externally applied magnetic field $\mathbf{H}$ with a flux density $\mathbf{B} = \mu_0 \mathbf{H}$, where $\mu_0 = 4\pi \times 10^{-7} Tm/A$ for the permeability of vacuum. The torque that acts on the microrobot can be defined as

$$\mathbf{T} = V\mathbf{M} \times \mathbf{B}, \tag{1}$$

where $\mathbf{M}$ is the volume magnetization in A/m of the object of a certain volume V.

The force acting on the microrobot is described as

$$\mathbf{F} = V(\mathbf{M} \cdot \nabla)\mathbf{B}. \tag{2}$$

Assuming no electric current is flowing through the micro-robot, Maxwell's equation require that $\nabla \times \mathbf{B} = \mathbf{0}$, from which the force can be expressed as

$$\mathbf{F} = V \left[\frac{\partial \mathbf{B}}{\partial x} \ \frac{\partial \mathbf{B}}{\partial y} \ \frac{\partial \mathbf{B}}{\partial z} \right]^T \mathbf{M}. \tag{3}$$

These equations are dependent on the magnetization and volume of a microrobot. The normalized force and torque can, however, be expressed by a normalized volume magnetization $\tilde{\mathbf{M}}$.

The magnetic field throughout the workspace of a set of static electromagnets can be computed at point $\mathbf{P}$ for any given electromagnet e. The magnetic field due to this electromagnet can be expressed as the vector $\mathbf{B}_e(\mathbf{P})$, whose magnitude varies linearly with the current through the electromagnet. When assuming an ideal soft-magnetic material with negligible hysteresis and keeping the cores within their linear magnetization regions, the field contributions of the individual currents superimpose linearly. This can be expressed as the $3 \times n$ unit-field contribution matrix $\mathcal{B}(\mathbf{P})$

$$\mathbf{B}(\mathbf{P}) = \left[\tilde{\mathbf{B}}_1(\mathbf{P}) \ldots \tilde{\mathbf{B}}_n(\mathbf{P}) \right] \begin{bmatrix} i_1 \\ \vdots \\ i_n \end{bmatrix} = \mathcal{B}(\mathbf{P})I, \tag{4}$$

where vector I represents the current in each of n coils.

The derivative of the magnetic field in a given direction in a specific frame, for example the direction x, can be expressed as the contributions from each of the currents

$$\frac{\partial \mathbf{B}(\mathbf{P})}{\partial x} = \left[\frac{\partial \tilde{\mathbf{B}}_1(\mathbf{P})}{\partial x} \ldots \frac{\partial \tilde{\mathbf{B}}_n(\mathbf{P})}{\partial x} \right] \begin{bmatrix} i_1 \\ \vdots \\ i_n \end{bmatrix} = \mathcal{B}_x(\mathbf{P})I. \tag{5}$$

These equations can now be combined to form a $6 \times n$ actuation matrix $\mathcal{A}(\tilde{\mathbf{B}}, \mathbf{P})$ which depends on the orientation of the magnetic field and the set point

$$\begin{bmatrix} \mathbf{B} \\ \mathbf{F}_{unit} \end{bmatrix} = \begin{bmatrix} \mathcal{B}(\mathbf{P}) \\ \tilde{\mathbf{M}}^T \mathcal{B}_x(\mathbf{P}) \\ \tilde{\mathbf{M}}^T \mathcal{B}_y(\mathbf{P}) \\ \tilde{\mathbf{M}}^T \mathcal{B}_z(\mathbf{P}) \end{bmatrix} \begin{bmatrix} i_1 \\ \vdots \\ i_n \end{bmatrix} = \mathcal{A}(\tilde{\mathbf{B}}, \mathbf{P}) I. \quad (6)$$

For a desired target vector, (6) can be solved via the pseudo-inverse

$$I = \mathcal{A}(\tilde{\mathbf{B}}, \mathbf{P})^\dagger \begin{bmatrix} \mathbf{B} \\ \mathbf{F}_{unit} \end{bmatrix}. \quad (7)$$

2.1 The MiniMag

The magnetic control system is the MiniMag system as described in (Schuerle et al., 2013). It consists of eight coils ($n = 8$) to generate a magnetic field of variable amplitude and direction. The eight electromagnets are designed in a tilted arrangement, thereby occupying only a single hemisphere, which allows the incorporation of the MiniMag into a microscope system. The system is capable of 5-DOF wireless control of micro- and nano-structures (3-DOF position, 2-DOF pointing orientation), within a spherical workspace with a diameter of approximately $10\ mm$. This allows for magnetic fields and field gradients up to $50\ mT$ and $5\ T/m$ at frequencies up to $2\ kHz$.

Furthermore, the system can generate stepping, oscillating and rotating magnetic fields enabling new approaches for actuation. Examples can be found in (Tung et al., 2014b) and (Frutiger et al., 2010), which presented a new generation of microrobots actuated by an oscillating field in the kHz range.

2.2 The RodBot

The microrobot, named the RodBot (see Fig. 3), is a wireless mobile device with a typical size of $50 \times 60 \times 300 - 600\ \mu m$. The polymer body of the robot contains several soft-magnetic posts (perpendicular to the long axis) which align with an external magnetic field. When the field direction changes, the RodBot realigns with it. When placed in a rotating magnetic field the RodBot rolls continuously on the supporting surface.

To increase the magnetization of its structure, the RodBot is designed as a rectangular polymer (SU-8) rod with internal, transverse soft-magnetic posts (see Fig. 3) consisting of a cobalt-nickel (CoNi) alloy. For the fabrication of the
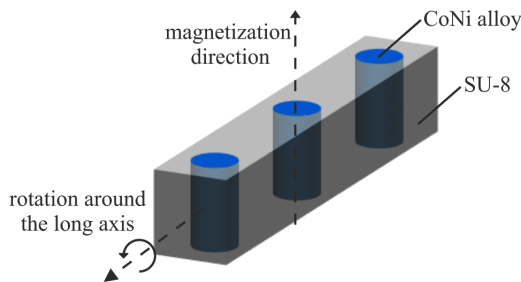

Fig. 3. The RodBot has a polymer body and soft-magnetic posts which align with an external magnetic field.

RodBot, a process was adapted that combines a photosensitive polymer with electroplated magnetic metals that offer good adhesion between the two materials. Details of this manufacturing process can be found in (Tung et al., 2013).

The RodBot rolls on a substrate in a low Reynolds number liquid environment and generates flows to lift up and trap crystals in a vortex above it. Protein crystals ranging from a few microns to several hundreds of microns in size can then be transported to and deposited onto an extraction-loop. Due to the design of the robot and the method of actuation (i.e., a rotating magnetic field induces a forward velocity), the system is limited to non-holonomic motion. This constraint implies that a direct sideways velocity is not possible, as can be identified for 'classical' unicycle mobile robots.

3. VISUAL CONTROL SYSTEM

A top camera observes the scene where image processing detects the position and orientation of the RodBot and provides feedback for the visual control system. Based on this initial state of the robot, obstacles to be avoided, and the final goal location and orientation, a smooth trajectory is generated. This control approach (trajectory tracking) incorporates the kinematic and non-holonomic constraints of the robot and enables a straight-forward design of motion. The control input to the system is the forward velocity of the robot (a rotating magnetic field) and the yaw angle of the robot (the angle of the magnetic field).

3.1 Kinematic modelling

The configuration vector is defined as $\mathbf{q} = [x,\ y,\ \theta]^T$. Trajectory tracking is solved by considering the forward velocity of the robot, v, and the steering angle of the robot, θ. As presented in Fig. 4, let P be an arbitrary point on the trajectory and Q be the center of mass of the RodBot. With respect to an inertial reference frame $\{I\}$, Q and P are denoted as $Q_{\{I\}} = [q_x,\ q_y,\ 0]^T$ and $P_{\{I\}} = [p_x,\ p_y,\ 0]^T$. A Cartesian error between the RodBot and the trajectory is then defined as $\mathbf{e}(\mathbf{q}) = P - Q$. The goal of the visual control system is to drive this error to zero.
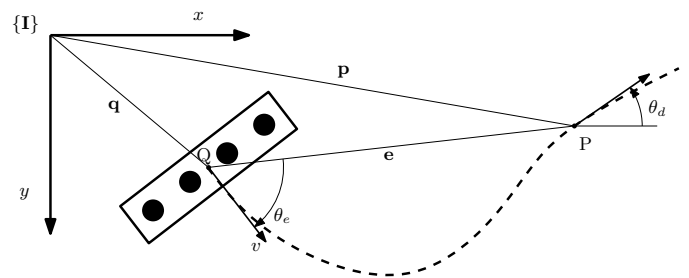

Fig. 4. The center of mass of the RodBot is denoted by Q. An arbitrary point on the trajectory is denoted by P. The visual control system is designed to drive the error $\mathbf{e}(\mathbf{q}) = P - Q$ to zero.

3.2 Motion Planning

As mentioned in section 2.2, the robot is unable to move directly sideways (i.e., the non-holonomic constraint) and

cannot rotate around its vertical axis without a forward motion. These limitations are integrated in a trajectory that is designed based on the measured state of the robot.

A 2D planar trajectory is generated with two polynomial functions. Due to the simplicity of incorporating constraints on a local level (i.e., on individual points and their time derivatives) as well as on a global level (i.e., constraints on the complete trajectory and its time derivatives), polynomial trajectory generation is used. A trajectory of order m is defined as:

$$q(t) = a_0 + a_1 t + a_2 t^2 + \ldots + a_m t^m, \tag{8}$$

with $t \in [t_i, \ t_f]$, where t_i indicates the initial time instant ($t = 0$) and t_f indicates the final time instant. A general solution is acquired by solving a system of linear equations:

$$\mathbf{Ta} = \mathbf{q}_c, \tag{9}$$

where $\mathbf{T}$ is the so-called Vandermonde matrix (Biagiotti and Melchiorri, 2008). The unknown polynomial coefficients are $\mathbf{a} = [a_0, \ a_1, \ldots, \ a_m]^T$, and $\mathbf{q}_c$ lists the ($m + 1$) constraints that the polynomial should satisfy. The coefficients in $\mathbf{a}$ can be computed as

$$\mathbf{a} = \mathbf{T}^\dagger \mathbf{q}_c, \tag{10}$$

where $\mathbf{T}^\dagger$ represents the pseudo-inverse of $\mathbf{T}$.

A 5th order polynomial is chosen, which implies a $\mathcal{C}^2$ continuous point-to-point trajectory. This satisfies the requirements for a smooth and varying trajectory and does not excessively excite the motion system (Flash and Hogan, 1985). One advantage of a polynomial trajectory is the ease of incorporating the non-holonomic constraint via an initial velocity. Similarly, an angle of approach (a final orientation) can be included.

3.3 Kinematic controller

As the trajectory takes the non-holonomic constraint of the robot into account, we employ the following controller:

$$\theta_c = \arctan\left(\frac{e_y}{e_x}\right),$$

$$v_c = v_{max} \tanh\left(\frac{\|v_d\|}{k_v}\right), \tag{11}$$

where $e_y = p_y - q_y$, $e_x = p_x - q_x$ and $\|v_d\| = \sqrt{e_x^2 + e_y^2}$. As shown in Fig. 4, $P = [p_x, \ p_y]^T$ is the desired position of the robot (defined by the user or determined by vision) and $Q = [q_x, \ q_y]^T$ is the current, measured position of the robot. Tuning parameters for the forward velocity of the RodBot include v_{max} and $k_v > 0$.

4. EXPERIMENTAL EVALUATION

The experimental system is shown in Fig. 5. This includes the MiniMag for magnetic field generation, a microscope with camera for visual feedback, a soaking dish that contains the RodBot and the crystals, and a desktop PC for processing. The RodBot used for experiments contained five soft-magnetic posts and has a length of 300 μm. Typically, crystals have a size of $50 - 300$ μm and are submersed in a cryoprotectant buffer.
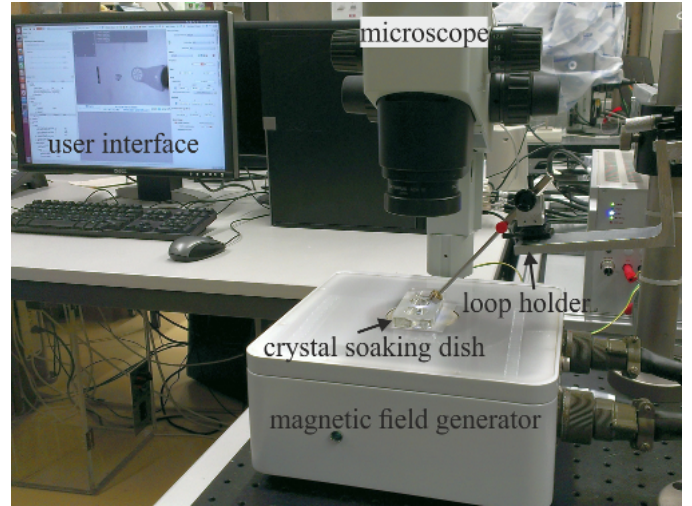

Fig. 5. The experimental system contains the eight-coil magnetic field generator, a microscope with camera for visual feedback and a desktop PC for processing.

4.1 Magnetic Actuation

The motion of the RodBot was evaluated in solutions of different viscosities (Tung et al., 2014a). In particular, the RodBot was tested in DI water (viscosity of $1\ mPa{\cdot}s$), 10% and 20% polyethylene glycol (PEG) solutions (viscosity of $4.7\ mPa \cdot s$ and $9.28\ mPa \cdot s$ respectively). Fig. 6 shows the forward velocity of the RodBot in these three solutions for different frequencies of the magnetic field. If the RodBot rolls without slipping, the forward velocity equals the rod perimeter times the rotational frequency. The deviation of the experimental data from this ideal forward velocity indicates slippage of the RodBot. At higher forward velocity and higher viscosity the fluidic drag forces increase, and, thus, the slippage increases.
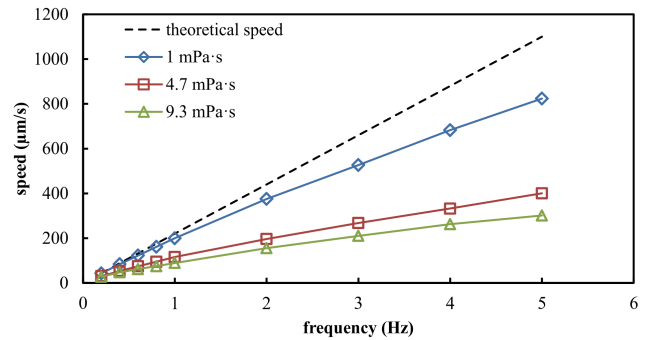

Fig. 6. The forward velocity of the RodBot actuated in water and in PEG solutions in fields rotating at different frequencies (field strength 5 mT).

4.2 Visual Feedback

For visual feedback, a PointGrey Grasshopper 50S5C CCD Firewire camera is used, which is fitted to an Olympus SZX-9 microscope. The image frame size is set to 640×480 pixels with an effective pixel size of 6 μm. The images are extracted at a rate of 30 frames per second and processed with the computer vision library OpenCV. Successful

detection and tracking of the RodBot is achieved by tracking the circular soft-magnetic posts of the robot. A blob detection algorithm finds the posts and determines from these the position and orientation of the RodBot. This can be seen in Fig. 7 where the white circles depict each individually detected soft-magnetic post. An observer (Kalman filter) is used to smooth the measurements and filter out any outliers. The accuracy of tracking is limited by the resolution of the camera and the optics, and has been found to be less than 1 px for the position and less than 1° for the orientation. The entire system is controlled through C++ by a single computer with an Intel Core 2 Quad CPU Q9650 3.0 GHz processor running Ubuntu Linux. This enabled a control rate of the magnetic field of 1 kHz.

4.3 Control Evaluation

The controller described by (11) directs the robot towards the goal at all times. The forward velocity of the robot is dependent on the trajectory as well as the current position. As such, the input velocity is similar to the velocity of the designed trajectory, allowing a kinematic constraint (e.g., a maximum acceleration) to be easily incorporated.

Fig. 7 shows the results of trajectory tracking. The white solid line depicts the desired trajectory, the blue solid line the executed motion of the robot (filtered with a Kalman filter). The blue points depict the position of the robot, measured with the visual tracking system. The deviation of the desired and executed trajectory stays within 15 px or 90 μm. Furthermore, it can be seen that the initial velocity of the robot takes the non-holonomic constraint into account. For both trajectory tracking experiments the maximum frequency of the rotating magnetic field does not exceed 3.5 Hz. This corresponds to a maximum forward velocity of 600 $\mu m/s$. The control parameters are set as $v_{max} = 10$ and $k_v > 0.01$

4.4 Protein Crystal Trapping and Transporting

To evaluate the visual control method for crystal trapping and transportation the robot was submersed in a cryoprotectant buffer containing several protein crystals. Following detection of the robot by the tracking system, a trajectory was planned through the position of the crystal towards a final position. In order to successfully trap and release a crystal, the forward velocity of the RodBot should be sufficiently high (i.e., $v > 200$ $\mu m/s$). Furthermore, when releasing the crystal the RodBot should come to a standstill and then move away slowly in order to avoid inducing further motion or trapping of the crystal due to fluid flow. The success rate of crystal trapping and transportation is high, and not limited to the size of the crystals.

Snapshots of this procedure are shown in Fig. 8. Clockwise (starting from top-left) the figures show the following. 1: The RodBot with the generated trajectory. In this, the via-point is the position of the crystal. 2: The RodBot approaching the crystal (via-point) with sufficiently high forward velocity. 3: The rising flow in front of the RodBot lifts up the crystal. 4: The vortex above the RodBot traps and transports the crystal to the final position. 5: The RodBot slows down to a lower velocity to release the
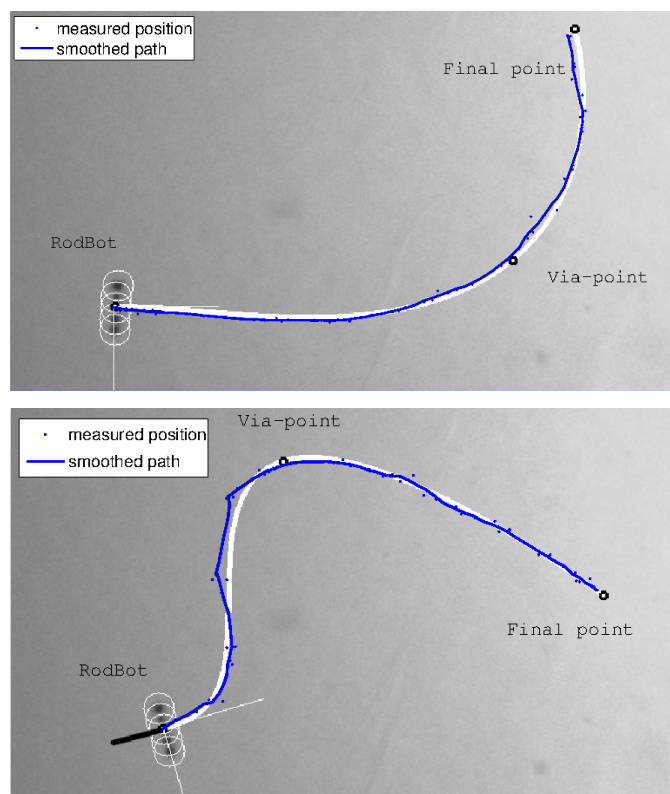

Fig. 7. Visual trajectory tracking of the RodBot for two different trajectories (with via-point) in water. The deviation between generated (white) and measured (blue) trajectory does not exceed 15 px or 90 μm.

crystal. 6: The crystal is released at the final point of the trajectory, and the RodBot moves away.

5. CONCLUSION

In this work we presented a microrobot, a magnetic actuation system and a visual control system for automated protein crystal harvesting. The microrobot is transversely magnetized and can roll around its long axis on a surface, generating a vortex above it to trap and transport microobjects. The motion of the robot is controlled with visual feedback and a smooth trajectory to incorporate the kinematic and non-holonomic constraints. We show the successful automated trapping, transportation and releasing of protein crystals via our non-contact micromanipulation method.

This approach enables a fast and gentle extraction of crystals from soaking dishes/wells where damage due to the handling of crystals is minimized. We foresee that this system can be easily integrated into larger crystal manipulation and harvesting platforms for the automation of this delicate process.

REFERENCES

Banerjee, A., Gupta, S., 2013. Research in automated planning and control for micromanipulation. IEEE Transactions on Automation Science and Engineering 10 (3), 485–495.
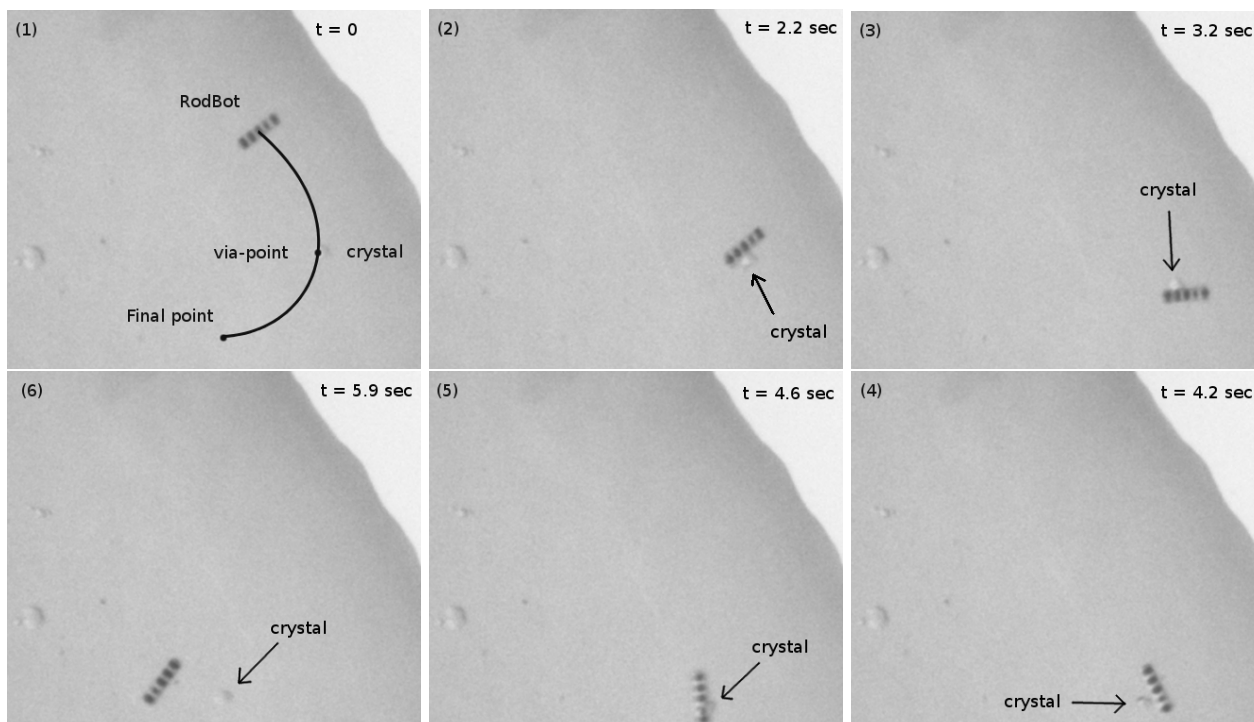
Fig. 8. Snapshots of the automated crystal harvesting process. The magnetically actuated microrobot (the RodBot) follows a predefined vision-based trajectory, where the via-point is determined as the position of the crystal (1). A sufficiently high forward velocity of the RodBot is necessary to create a rising flow in front of it (2). The crystal gets lifted up by this rising flow (3). The motion of the RodBot creates a vortex above it to trap and transport the crystal (4). The RodBot transports the crystal to the final point of the trajectory (5). The crystal is released and the RodBot moves away (6).

Biagiotti, L., Melchiorri, C., 2008. Trajectory Planning for Automatic Machines and Robots. Springer Berlin Heidelberg.

Deller, M. C., Rupp, B., 2014. Approaches to automated protein crystal harvesting. Acta Crystallographica Section F 70 (2), 133–155.

Diller, E., Ye, Z., Sitti, M., 2011. Rotating magnetic micro-robots for versatile non-contact fluidic manipulation of micro-objects. In: IEEE/RSJ Int. Conf. on Intelligent Robots and Systems (IROS). pp. 1291–1296.

Flash, T., Hogan, N., 1985. The coordination of arm movements: an experimentally confirmed mathematical model. Journal of Neuroscience 5 (7), 1688–1703.

Frutiger, D. R., Kratochvil, B. E., Vollmers, K., Nelson, B. J., 2010. Small, fast, and under control: wireless resonant magnetic micro-agents. International Journal of Robotics Research 29 (5), pp. 613–636.

Jiang, G.-L., Guu, Y.-H., Lu, C.-N., Li, P.-K., Shen, H.-M., Lee, L.-S., Yeh, J. A., , Hou, M. T.-K., 2010. Development of rolling magnetic microrobots. Journal of Micromechanics and Microengineering 20 (085042).

Laumond, J.-P., 1998. Robot Motion Planning and Control. Springer-Verlag, Berlin.

Schuerle, S., Erni, S., Flink, M., Kratochvil, B., Nelson, B., 2013. Three-dimensional magnetic manipulation of micro- and nanostructures for applications in life sciences. IEEE Trans. on Magnetics 49 (1), 321–330.

Staub, C., Lenz, C., Jensen, B., Can, S., Knoll, A., Bauernschmitt, R., 2012. Micro camera augmented endoscopic instruments: Towards superhuman performance in remote surgical cutting. In: IEEE/RSJ Int. Conf. on In-

telligent Robots and Systems (IROS). pp. 2000–2006.

Tung, H.-W., Maffioli, M., Frutiger, D., Sivaraman, K., Pane, S., Nelson, B., Feb 2014a. Polymer-based wireless resonant magnetic microrobots. IEEE Transactions on Robotics 30 (1), 26–32.

Tung, H.-W., Peyer, K. E., Sargent, D. F., Nelson, B. J., September 2013. Noncontact manipulation using a transversely magnetized rolling robot. Applied Physics Letters 103 (11), 114101.

Tung, H.-W., Sargent, D. F., Nelson, B. J., 2014b. Protein crystal harvesting using the RodBot: a wireless mobile microrobot. Journal of Applied Crystallography 47 (2).

Viola, R., Carman, P., Walsh, J., Miller, E., Benning, M., Frankel, D., McPherson, A., Cudney, B., Rupp, B., 2007. Operator-assisted harvesting of protein crystals using a universal micromanipulation robot. J. of Applied Crystallography 40, 539–545.

Wagner, A., Duman, R., Stevens, B., Ward, A., Jul 2013. Microcrystal manipulation with laser tweezers. Acta Crystallographica Section D 69 (7), 1297–1302.

Yaser, M., Khajepour, H., Lebrette, H., Vernede, X., Rogues, P., Ferrer, J.-L., 2013. A geometrical approach for semi-automated crystal centering and *in situ* X-ray diffraction data collection. Journal of Applied Crystallography 46 (3), 740–745.

Zhang, L., Petit, T., Peyer, K. E., Nelson, B. J., 2012. Targeted cargo delivery using a rotating nickel nanowire. Nanomedicine: Nanotechnology, Biology, and Medicine 8, pp. 1074–1080.